Negative Thermal Expansion in Cubic $FeFe(CN)_6$ Prussian Blue Analogues

Received 00th January 20xx,
Accepted 00th January 20xx

DOI:

Naike Shi,[a, b] Qilong Gao,[a, b] Andrea Sanson,[c] Qiang Li,[a,b] Longlong Fan,[d] Yang Ren,[e] Luca Olivi,[f] Jun Chen *[a, b] and Xianran Xing [a, b]

Negative thermal expansion (NTE) behavior is an interesting physical phenomenon, but the number of NTE materials is limited. In this study, a new NTE compound has been found, $FeFe(CN)_6$ Prussian blue analogue, where the average linear coefficient of thermal expansion (α_l) is -4.260×10^{-6} K^{-1} between 100 and 450 K. The NTE property and local vibration dynamics have been investigated by joint experiments of synchrotron X-ray diffraction, X-ray pair distribution function, and extended X-ray absorption fine structure. It has been observed that the Fe-C/Fe-N bonds expand with increasing temperature, while the unit cell shrink in $FeFe(CN)_6$. Both vibration directions of Fe-C and Fe-N prefer to be perpendicular to the linkage of Fe-C≡N-Fe rather than to be parallel. More evidences indicate that the transverse vibrations of N atoms dominate the NTE behavior of $FeFe(CN)_6$. The present results prove directly that the transverse thermal vibrations of C and N atoms are crucial for the occurrence of NTE of Prussian blue analogues.

Introduction

Most materials increase in volume upon heating on account of the inherent anharmonicity of bond vibrations. However, negative thermal expansion (NTE) compounds show unconventional volume contraction with increasing temperature. [1, 2]The intriguing NTE property could solve a number of problems caused by the mismatch of coefficients of thermal expansion (CTE) in a large number of technological and industrial applications. [3] The study on the nature of NTE materials has made a great progress in the recent two decades. [4-11] Some NTE mechanisms have been investigated, such as magnetovolume effect, [8, 12 - 14] low-frequency phonons, [7, 15-17] and valence transition. [10,18 - 19] In recent years, an increasing amount of NTE materials driven by the population of low-energy phonon modes have been reported, such as AM_2O_8 (e.g. ZrW_2O_8, $ZrMo_2O_8$), [20 - 22] AM_2O_7(e.g. ZrV_2O_7), [4] fluorides, [23 - 25] and Prussian blue analogues (PBAs). [16, 26] All these materials possess open framework structures, consisting of corner sharing tetrahedral or octahedral units. This characteristic crystal structure is widely believed in being correlated with the NTE behaviour. However, the intrinsic NTE mechanisms remain debate. For the prototype of NTE compound ZrW_2O_8, the rigid unit mode (RUM) suggests that ZrO_6 and WO_4 are rigid, and the thermal contraction of lattice volume originates from the related rocking motion. [27] The tent model describes the translation of WO_4 units into empty space rather than a significant transverse motion of corner-linking atom, which is responsible for its NTE. [20] In some open framework structure materials, the concepts of "guitar-string" effect and tension effect have been proposed to explain the NTE mechanism, [17, 21] in which the transverse vibration motion plays a key role.

Similar to those NTE oxides, the structure of cyanide-based molecular framework materials have more flexible linkages M_1-C≡N-M_2 and possess framework with large open space. Benefitting from the special structure characters, PBAs have wide applications as multifunctional materials in catalysis, [28] energy storage, [29] battery materials, [30] drug delivering, [31] and so on. Especially, some PBAs show NTE property. For instance, in 1997, $Zn(CN)_2$ was determined firstly that it has larger lattice parameter at 14K than at 305K. [32] In 2004, Margadonna et al [33] reported $FeCo(CN)_6$ PBAs exhibit nearly zero thermal expansion in the range of 4.2 to 300 K. NTE has been found in some PBAs, including $M^{II}Pt^{IV}(CN)_6$, [34, 35] M^{II}_3 $[Co^{III}(CN)_6]_2$, M^{II}_2 $[Fe^{II}(CN)_6]_2$, [36] $Ag_3Co(CN)_6$, [7] $LnCo(CN)_6$, [37] $YFe(CN)_6$ [16] and $GaFe(CN)_6$. [38] However, the NTE behaviours in many PBAs are anisotropic, while isotropic thermal contraction in PBAs needs to be unexposed.

In this work, we have found out that $FeFe(CN)_6$ shows isotropic NTE property in a large temperature range. In the past, $FeFe(CN)_6$ has been extensively studied as electrode materials, [39, 40] but its NTE property has never been observed. Herein, the NTE mechanism of $FeFe(CN)_6$ has been investigated by using high-resolution synchrotron X-ray diffraction (SXRD), pair distribution function (PDF), and extend X-ray absorption fine structure (EXAFS). The key factor contributing to the NTE behaviour in $FeFe(CN)_6$ resides in the transverse vibrations of the C≡N chemical bonds, with a major contribution from N atoms. This work not only expands the scope of isotropic NTE materials, but also provides an explicit rationale of the local vibrational dynamics triggering NTE behaviour.

[a.] Beijing Advanced Innovation Center for Materials Genome Engineering, University of Science and Technology Beijing, Beijing 100083, China.
[b.] Department of Physical Chemistry, University of Science and Technology Beijing, Beijing 100083, China.
[c.] Department of Physics and Astronomy, University of Padova, Padova I-35131, Italy.
[d.] College of Physics and Materials Science, Tianjin Normal University, Tianjin 300387, China.
[e.] Argonne National Laboratory, X-ray Science Division, Argonne, Illinois 60439, United States.
[f.] Elettra Sincrotrone Trieste, 34149 Basovizza, Italy.
† Footnotes relating to the title and/or authors should appear here.
Electronic Supplementary Information (ESI) available: [details of any supplementary information available should be included here]. See DOI: 10.1039/x0xx00000x

Experimental section

Materials

The sample of $FeFe(CN)_6{\bullet}1.9H_2O$ was fabricated by a simple solution precipitation method. The precursor of potassium ferricyanide ($K_3Fe(CN)_6$) and hydrochloric acid (HCl) was purchased from Aladdin (Shanghai, China) and Sinopharm Chemical ReagentCo., Ltd (Shanghai, China), respectively. All chemical reagents were analytical grade and used without further purification.

Preparation of FeFe(CN)6

To prepare the powder of $FeFe(CN)_6{\bullet}1.9H_2O$, 50 mL of 0.1 mol/L HCl was prepared firstly, then 10 mmol of $K_3Fe(CN)_6$ was added in it. The mixture solution was stirred under room temperature for 10 minutes, which was then heated to 355 K and further stirred for 12 hours. The precipitates were yielded which were then centrifuged, filtered, and washed for several times with deionized water and ethanol. The powder samples of $FeFe(CN)_6{\bullet}1.9H_2O$ were dried at 335 K in air for 10 hours. To obtain the dehydrated sample of $FeFe(CN)_6$, the sample of $FeFe(CN)_6{\bullet}1.9H_2O$ was heated at 475 K in inert gas for an hour.

Characterization

Sample Characterizations

In order to investigate crystal structure of $FeFe(CN)_6$, temperature dependence of high-resolution synchrotron XRD (SXRD) was employed in the temperature range from 100 to 450K at the 11-BM-B beamline of Advanced Photon Source (APS). The light wavelength was 0.412634 Å. The crystal structure was refined by the Rietveld method using FULLPROF software based on a cubic ($Fm\bar{3}m$) model. Pair distribution function (PDF) analysis of G(r) under various temperatures was performed at the beamline 11 -ID-C of APS (λ = 0.1173 Å). The G(r) functions were computed from the total scattering data using PDFgetX2. $G(r) = 4\pi r\,[\rho(r) - \rho_0]$ where $\rho(r)$ and ρ_0 are the instantaneous and average densities [41]. The G(r) curves were converted to a radial distribution function R(r), $[R(r) = r(G(r) + 4\pi r\rho_0)]$, to determine the temperature dependence of the peak distance positions. The morphology of the sample was examined using field-emission scanning electron microscope (FE-SEM, SUPRA-40, Carl Zeiss) and transmission electron microscope (TEM, JEOL JEM-2010 at 200kV). Thermal stability of $FeFe(CN)_6{\cdot}1.9H_2O$ was measured in an Ar condition with a heating rate of 1 K/min by thermogravimetric-differential scanning calorimetry analysis (TG-DSC) (Labsys™ Evo, Setaram Corp.).

EXAFS Measurements

For EXAFS measurements, the $FeFe(CN)_6$ powder was mixed with boron nitride, and shaped into circle slice under uniaxial pressure. To have an absorption edge jump $\Delta\mu x$~1, the concentration of sample powder was adjusted. The Fe K-edge EXAFS spectra in $FeFe(CN)_6$ were collected in transmission mode at the XAFS beamline of ELETTRA synchrotron in Trieste (Italy), where the x-ray beam was monochromatized by a Si (111) double-crystal monochromator and the storage ring was operated with electron energy of 2.4 GeV. The EXAFS data was collected under declining temperature from 475 K to 300 K with a step of 35 K. In terms of obtaining a uniform wave vector step Δk~0.035 $Å^{-1}$, each spectrum was collected in the energy range of 6.8-8.4 keV, with an energy step varying from 0.2 eV in the near-edge region to the highest energies about 4.7 eV. Herein, two spectra were collected at each temperature point. During the entire experiment, the samples were mounted in a high-temperature furnace under high-vacuum (10^{-5} mbar), and the temperature was stabilized and monitored through an electric heater controlled by a feedback loop, ensuring a thermal stability within ±1 K.

Results and discussion

The sample of $FeFe(CN)_6{\bullet}1.9H_2O$ was prepared simply by a solution precipitation method. Adding $K_3Fe(CN)_6$ in acid solution at a heated temperature of 355 K and keeping stirring for 12 hours. The as-prepared sample presents dark blue in color. The FE-SEM and TEM images of the samples exhibit clearly that they are made up of nanocubes with a uniformly distributed size of ~250-300nm (Fig. 1a, b). The selected area electron diffraction (SAED) pattern (the inset in Fig. 1b) exhibits the single crystal spot pattern of cubic symmetry from the [001] zone axis, revealing that each cube is a well-crystalline single crystal. The TG-DSC analysis reveals 9.19 weight % water in the sample, amounting to 1.9 water molecules per $FeFe(CN)_6$ unit (Fig. S1). The valence state of Fe in the sample is determined to be +3 by the XANES spectra (Fig. S2) Accordingly, the chemical composition of the present sample should be expressed as $FeFe(CN)_6{\bullet}1.9H_2O$. Keeping $FeFe(CN)_6{\bullet}1.9H_2O$ at 475 K in inert atmosphere, the dehydrated sample of $FeFe(CN)_6$ can be obtained.

The crystal structure of dehydrated $FeFe(CN)_6$ was determined by high-resolution SXRD. The structure refinement of $FeFe(CN)_6$ can be performed with the structure model of centrosymmetric $Fm\bar{3}m$ space group (Fig. S3). Fig. 2a demonstrates that the framework structure of $FeFe(CN)_6$ consists of FeC_6 and FeN_6 octahedron. Each octahedron is linked with the C≡N linear bridges, which build a flexible 3D cubic network. It is found that the lattice constant of dehydrated $FeFe(CN)_6$ is 10.189 Å at room temperature, which is smaller than that of $FeFe(CN)_6{\bullet}1.9H_2O$ (10.202 Å).

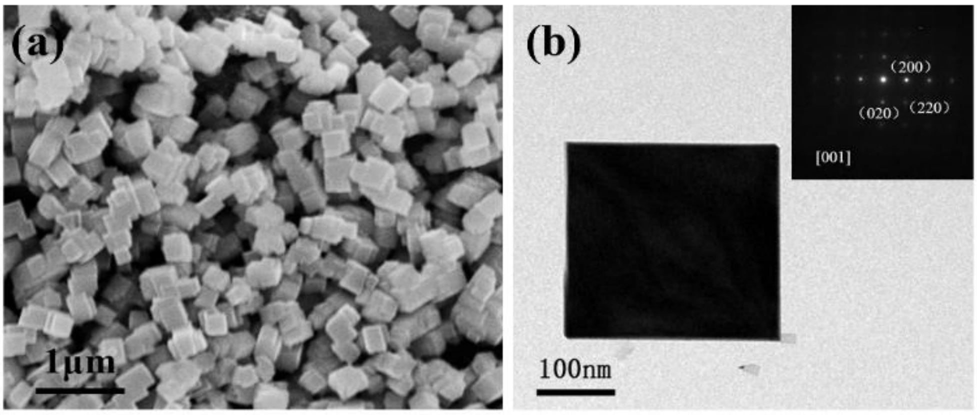

Figure 1 (a) SEM image of $FeFe(CN)_6 \bullet 1.9H_2O$, and (b) TEM image of a single crystal of $FeFe(CN)_6 \bullet 1.9H_2O$. The inset is the SAED pattern.

The temperature dependence of high-resolution SXRD patterns was collected to determine lattice constant of $FeFe(CN)_6$ at various temperatures. As illustrated in Fig. 2b, $FeFe(CN)_6$ shows an interesting isotropic NTE property. The CTE of $FeFe(CN)_6$ is observed to be approximately linear over the whole temperature range 100 – 450 K, with an average linear CTE (α_l) value of about -4.26 × 10^{-6} K^{-1}. Compared with other framework structure isotropic NTE materials (Table S1), the absolute CTE value of $FeFe(CN)_6$ is moderate. It is a half of that of ZrW_2O_8 (-8.7 × 10^{-6} K^{-1}, 20 - 430 K), [42] and just one fifth that of $Cd(CN)_2$ (-20.4 × 10^{-6} K^{-1} , 150 - 375 K); [43] It is much stronger than other PBAs such as $Fe[Co(CN)_6]$ (-1.47 × 10^{-6} K^{-1}, 4.2 - 300 K) [33] and $Ni[Pt(CN)_6]$ (-1.02 × 10^{-6} K^{-1}), [44] while comparable to $Ga[Fe(CN)_6]$ (-3.95 × 10^{-6} K^{-1}, 100 - 475 K) [38] and $Fe[Pt(CN)_6]$ (-4 × 10^{-6} K^{-1}). [44]

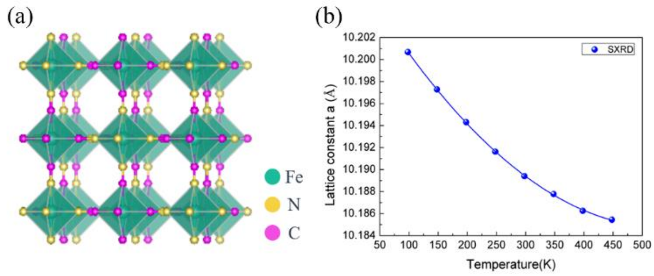

Fig. 2 (a) The framework structure of $FeFe(CN)_6$. (b) Temperature dependence of lattice constant determined by high-resolution SXRD

Through the SXRD measurement, we derive also other crystal structure information such as bond length. Because the scattering factor of C and N atoms are small and similar, it is too difficult to distinguish atomic displacements of C and N in $FeFe(CN)_6$. To obtain a convergent and reasonable refinement, Fe-C and Fe-N bonds were restricted to be equal in the present study. As a result, the temperature dependence of the bonds lengths exhibit an unphysical compression limited to crystallographic symmetry constrains (Fig. 3c). That is because SXRD is sensitive to the average long-range crystal structure rather than the correlations of atom pair motions. It is known that bond lengths measured by the diffraction method are the distances between the average positions of atoms [2]， which is named "apparent" bond length (Fig. 3d). Whereas, we intend to acquire information on the bond distance taking into account the atom-atom correlation, called "true" bond length, which can deviate from the local structure. Accordingly, in order to investigate the NTE mechanism of $FeFe(CN)_6$, temperature dependence of synchrotron X-ray PDF and EXAFS investigations were carried out. Not only the "true" bond length of instantaneous structure can be uncovered, but also

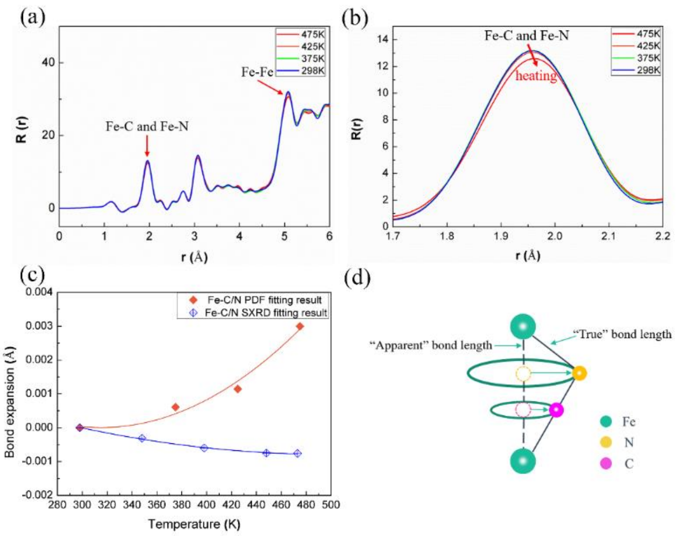

Fig. 3 (a) Temperature dependence of X-ray PDF radial distribution function, R(r), from 298K to 475K. (b) The distinct peak corresponding to Fe-C and Fe-N atomic pairs. (c) A comparison of Fe-C/N bond lengths as a function of temperature result from X-ray PDF and SXRD. Lines are a guide for eyes. (d) Schematic representation of the atomic linkage of vibrations related to NTE of $FeFe(CN)_6$.

the magnitude of displacement of bridging atoms can be determined.

The atom linkages Fe-C/Fe-N and Fe⋯Fe can be discriminated as shown in Fig. 3a. The shifting of peak position in the R(r) as function of temperature indicates the change of the correlated "true" bond length of Fe-C/Fe-N (Fig. 3b). The "true" bond length of Fe-C/Fe-N is around 1.95 Å, which is nearly equal to that of Ga-N/Fe-C in $GaFe(CN)_6$, [38] and slightly smaller than that of Zn-C/N in $Zn(CN)_2$ (2.02 Å) [45] and Sc-F in

ScF_3 (2.0 Å). [17] It is interesting to observe that the PDF peak position shifts to higher r with increasing temperature, attesting that the pair distance of Fe-C/Fe-N expands upon heating, which is opposite to the result of SXRD (Fig. 3c). It should be mentioned that it is improbable to distinguish the Fe-C and Fe-N bonds by the present PDF data, since the length difference between these two kinds of bonds is less than 0.1 Å. Due to the relatively low intensity correlations between carbon and nitrogen atoms to those of Fe, local structural information of C/N cannot be extracted accurately. Less agreement in the low r range of G(r) results in the difficulty of obtaining accurate and more structure information by PDF (Fig. S4).

To overcome above shortages of PDF, temperature dependent Fe K-edge EXAFS measurements were performed. The true bonds length of Fe-C and Fe-N can be distinguished by EXAFS. Fig. 4a and 4b show the comparison of high-resolution SXRD and EXAFS results of the Fe-C and Fe-N bond length as function of temperature. It is interesting to observe that both the true Fe-C and Fe-N bonds lengths measured by EXAFS expand with increasing temperature, in accordance with the PDF results, while the apparent bonds lengths measured by high-resolution SXRD shrink. The CTE values for "apparent" Fe-C and Fe-N bonds are both -2.30×10^{-6} K^{-1}. In contrast, they are about $+1.42 \times 10^{-5}$ K^{-1} and $+2.97 \times 10^{-5}$ K^{-1} for the "true" Fe-C and Fe-N bonds, respectively.

This opposite thermal expansion behavior can be explained in terms of local vibrational dynamics, and can be related to the presence of large transverse atomic vibrations. [17] The temperature-dependence of the atomic mean square relative displacements (MSRDs), parallel and perpendicular to Fe-C and Fe-N chemical bonds were determined by the present EXAFS and SXRD (Fig. 4c, d). [17] As figures show, the perpendicular $MSRD_{\perp}$ for Fe-C and Fe-N are much larger than the parallel $MSRD_{||}$, which demonstrates the existence of large transverse relative vibrations of C≡N bonds. Especially, the relative anisotropic thermal vibrations have been estimated from the ratio of $MSRD_{\perp}$ and $MSRD_{||}$, $\gamma = MSRD_{\perp} / MSRD_{||}$. Fig. 4e displays the comparison of γ between Fe-C and Fe-N bonds as function of temperature. At 475 K the value of γ is 17 ± 5 for the Fe-C bond, while γ = 58 ± 16 for the Fe-N bond. The γ value of the Fe-N bond is much larger than that of some typical NTE compounds, like ZrW_2O_8 (γ = 26 - 32) [21] and ScF_3 (γ = 20), [17] and it is also larger than other PBAs like $GaFe(CN)_6$ (γ = 51 for Ga-N). [38] This indicates that longitudinal vibration amplitude of both Fe-C and Fe-N bonds are overwhelmed by transverse vibration amplitude, and the relative transverse vibrations of N atoms are more intense to the temperature and give the main

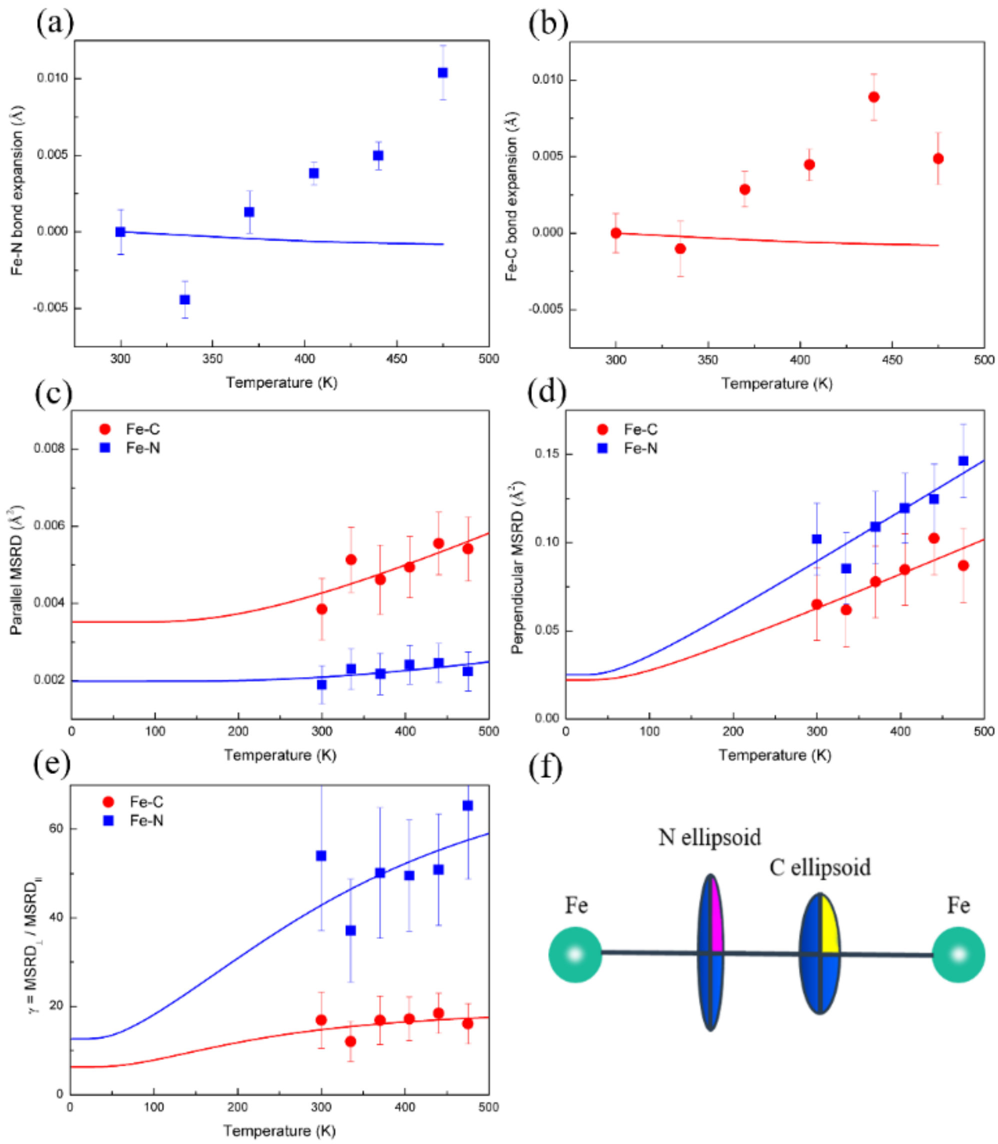

Fig. 4 Temperature dependence of Fe-N (a) and Fe-C (b) bond lengths result from SXRD (line) and EXAFS (symbols). Atomic MSRDs (c) parallel ($MSRD_{||}$) and (d) perpendicular ($MSRD_{\perp}$) to the bond direction, and the solid lines are the corresponding best-fitting Einstein models [46]. (e) Resulting anisotropy of the relative thermal vibrations of Fe-C and Fe-N atomic pairs. (f) Schematic view of the Fe–C and Fe–N relative thermal vibrations.

contribution to the NTE behavior of $FeFe(CN)_6$. Fig. 4f shows a schematic view of the vibrations schematic of the Fe-C and Fe-N atomic pairs. It can be seen that the transverse displacement of N is larger than that of C, as observed previously in $GaFe(CN)_6$ PBAs. [38] These results on the local vibrational dynamics are fully consistent with the presence of a "guitar-string" effect. [17] In the system of $FeFe(CN)_6$, C and N atoms in the middle of the Fe-C≡N-Fe linkage displace transversely, dragging Fe atoms at different sides to middle by Fe-C and Fe-N bonds forces, thus decreasing the distance between Fe and Fe atoms. This explains why the "apparent" bonds lengths of Fe-C and Fe-N decrease with increasing temperature, while the "true" bonds lengths of Fe-C and Fe-N increase.

Conclusions

In summary, in this work, we have discovered that $FeFe(CN)_6$ PBAs exhibits an isotropic NTE (with α_l = -4.26 × 10^{-6} K^{-1} between 100 and 450 K). The NTE mechanism of $FeFe(CN)_6$ has then been investigated with a combined approach, using high resolution SXRD, X-ray PDF, and EXAFS spectroscopy. Opposite trends between the "apparent" bonds and the "true" bonds for Fe-C and Fe-N as function of temperature have been observed, which can be related to the transverse vibrational motion of C≡N linkage. The measured MSRDs have provided quantitatively evidence that the motion perpendicular to the bonding direction is more preferred than that along the bonding direction. Concomitantly, the transverse vibration of N atoms is much more pronounced than C atoms, revealing the relative motion predominantly responsible for NTE in $FeFe(CN)_6$. The present work on this new NTE material $FeFe(CN)_6$, provides comprehensive and direct insight into the local vibrational dynamics of and demonstrates "guitar string" effect in cubic PBAs.

Conflicts of interest

There are no conflicts to declare.

Acknowledgements

This work was supported by the National Natural Science Foundation of China (Grant Nos. 21825102, 21731001, 21590793), the Fundamental Research Funds for the Central Universities, China (FRF-TP-17-001B), the Changjiang Young Scholars Award, and the National Program for Support of Top-notch Young Professionals. Use of the Advanced Photon Source, an Office of Science User Facility operated for the U.S. Department of Energy (DOE), Office of Science, by Argonne National Laboratory, was supported by the U.S. DOE under Contract No. DE-AC02-06CH11357. We acknowledge ELETTRA Synchrotron Light Laboratory for provision of synchrotron radiation (proposal number: 20175297), as well as the staff of XAFS Beamline for technical assistance. XANES data were collected on the 1W1B beamline at Beijing Synchrotron Radiation Facility (BSRF). We acknowledge the technical assistance of the beamline scientists Dr. Lirong Zheng (BSRF).

Notes and references

1 M. T. Dove and H. Fang. *Rep. Prog. Phys.*, 2016, **79**, 066503.
2 Z. Liu, Q. Gao, J. Chen, J. Deng, K. Lin and X. Xing, *Chem. Commun.*, 2018, **54**, 5164-5176.
3 J. Chen, L. Hu, J. Deng and X. Xing, *Chem. Soc. Rev.*, 2015, **44**, 3522-3567.
4 V. Korthuis, N. Khosrovani, A. W. Sleight, N. Roberts, R. Dupree and W. J. Warren, *Chem. Mater.*, 1995, **7**, 412-417.
5 G. Ernst, C. Broholm, G. R. Kowach and A. P. Ramirez, *Nature*, 1998, **396**, 147.
6 S. a Beccara, G. Dalba, P. Fornasini, R. Grisenti, A. Sanson and F. Rocca, *Phys. Rev. Lett.*, 2002, **89**, 025503.
7 A. L. Goodwin and C. J. Kepert, *Phys. Rev. B*, 2005, **71**, 140301.
8 X. G. Zheng, H. Kubozono, H. Yamada, K. Kato, Y. Ishiwata and C. N. Xu, *Nat. Nanotechnol.*, 2008, **3**, 724.
9 A. L. Goodwin, M. Calleja, M. J. Conterio, M. T. Dove, J. S. Evans, D. A. Keen, L. Peters and M. G. Tucker, *Science*, 2008, **319**, 794-797.
10 Y. W. Long, N. Hayashi, T. Saito, M. Azuma, S. Muranaka and Y. Shimakawa, *Nature*, 2009, **458**, 60.
11 L. Hu, J. Chen, L. Fan, Y. Ren, Y. Rong, Z. Pan, J. Deng, R Yun and X. Xing, *J. Am. Chem. Soc.*, 2014, **136**, 13566-13569.
12 S. Khmelevskyi, I. Turek and P. Mohn, *Phys. Rev. Lett.*, 2003, **91**, 037201.
13 K. Takenaka and H. Takagi, *Appl. Phys. Lett.*, 2005, **87**, 261902.
14 Y. Song, J. Chen, X. Liu, C. Wang, J. Zhang, H. Liu, K. Lin, S. Zhang and X. Xing, *J. Am. Chem. Soc.*, 2018, **140**, 602-605.
15 J. S. Evans, *J. Chem. Soc. Dalton*. 2014, **136**, 13566-13569.
16 Q. Gao, J. Chen, Q. Sun, D. Chang, Q. Huang, H. Wu, A. Sanson, R. Milazzo, H. Zhu, Q. Li, Z. Liu, J. Deng and X. Xing, *Angew. Chem.*, 2017, **129**, 9151-9156.
17 L. Hu, J. Chen, A. Sanson, H. Wu, C. Guglieri-Rodriguez, L. Olivi, Y. Ren, L. Fan, J. Deng and X. Xing, *J. Am. Chem. Soc.*, 2016, **138**, 8320-8323.
18 M. Azuma, W. T. Chen, H. Seki, M. Czapski, S. Olga, K. Oka, M. Mizumaki, T. Watanuki, N. Ishimatsu, N. Kawamura, S. Ishiwata, M. G. Tucker, Y. Shimakawa and J. P. Attfield, *Nat. Commun.*, 2011, **2**, 347.
19 J. Arvanitidis, K. Papagelis, S. Margadonna, K. Prassides and A. N. Fitch, *Nature*, 2003, **425**, 599.
20 F. Bridges, T. Keiber, P. Juhas, S. J. L. Billinge, L. Sutton J., Wilde and G. R. Kowach, *Phys. Rev. Lett.*, 2014, **112**, 045505.
21 A. Sanson, Chem. Mater., 2014, **26**, 3716-3720.
22 S. E. Tallentire, F. Child, I. Fall, L. Vella-Zarb, I. R. Evans, M. G. Tucker, D. A. Keen, C. Wilson and J. S. Evans, *J. Am. Chem. Soc.*, 2013, **135**, 12849-12856.
23 B. K. Greve, K. L. Martin, P. L. Lee, P. J. Chupas, K. W. Chapman and A. P. Wilkinson, *J. Am. Chem. Soc.*, 2010, **132**, 15496-15498.
24 J. Chen, Q. Gao, A. Sanson, X. Jiang, Q. Huang, A. Carnera, C. G. Rodriguez, L. Olivi, L. Wang, L. Hu, K. Lin, Y. Ren, Z. Lin, C. Wang, L. Gu, J. Deng, J. P. Attfield and X. Xing, *Nat. Commun.*, 2017, **8**, 14441.
25 L. Hu, F. Qin, A. Sanson, L. F. Huang, Z. Pan, Q. Li, Q. Sun, L. Wang, F. Guo, U. Aydemir, Y. Ren, C. Sun, J. Deng, G.

Aquilanti, J. M. Rondinelli, J. Chen, X. Xing and Y. Ren, *J. Am. Chem. Soc.*, 2018, **140**, 4477-4480.
26 T. R. Ravindran, A. K. Arora, S. Chandra, M. C. Valsakumar and N. C. Shekar, *Phys. Rev. B*, 2007, **76**, 054302.
27 M. G. Tucker, A. L. Goodwin, M. T. Dove, D. A. Keen, S. A. Wells and J. S. Evans, *Phys. Rev. Lett.*, 2005, **95**, 255501.
28 Q. Gao, J. Chen, Q. Li, J. Zhang, Z. Zhai, S. Zhang, R. Yu and X. Xing, *Inorg. Chem. Front.*, 2018, **5**, 438-445.
29 S. S. Kaye and J. R. Long, *J. Am. Chem. Soc.*, 2005, **127**, 6506-6507.
30 Y. You, X. L. Wu, Y. X. Yin and Y. G. Guo, *Energ. Environ. Sci.*, 2014, **7**, 1643-1647.
31 J. Li, F. Zhang, Z. Hu, W. Song, G. Li, G. Liang, J. Zhou, K. Li, Y. Cao, Z. Luo and K. Cai, *Adv. Healthc. Mater.*, 2017, **6**, 1700005.
32 D. J. Williams, D. E. Partin, F. J. Lincoln, J. Kouvetakis and M. O'Keeffe, *J. Solid. State. Chem.*, 1997, **134**, 164-169.
33 S. Margadonna, K. Prassides, and A. N. Fitch. *J. Am. Chem. Soc.*, 2004, **126**, 15390-15391.
34 A. L. Goodwin, K. W. Chapman and C. J. Kepert, *J. Am. Chem. Soc.*, 2005, **127**, 17980-17981.
35 K. W. Chapman, P. J. Chupas and C. J. Kepert, *J. Am. Chem. Soc.*, 2006, **128**, 7009-7014.
36 S. Adak, L. L. Daemen, M. Hartl, D. Williams, J. Summerhill and H. Nakotte, *J. Solid. State. Chem.*, 2011, **184**, 2854-2861.
37 S. G. Duyker, V. K. Peterson, G. J. Kearley, A. J. Ramirez-Cuesta and C. J. Kepert, *Angew. Chem.*, 2013, **125**, 5374-5378.
38 Q. Gao, N. Shi, Q. Sun, A. Sanson, R. Milazzo, A. Carnera, H. Zhu, S. H. Lapidus, Y. Ren, Q. Huang, J. Chen and X. Xing, *Inorg. Chem.*, 2018, **57**, 10918-10924.
39 X. Wu, W. Deng, J. Qian, Y. Cao, X. Ai and H. Yang, *J. Mater. Chem. A*, 2013, **1**, 10130-10134.
40 Q. Yang, W. Wang, H. Li, J. Zhang, F. Kang and B. Li, *Electrochim. Acta*, 2018, **270**, 96-103.
41 X. Qiu, J. W. Thompson and S. J. Billinge, *J. Appl. Crystallogr.*, 2004, **37**, 678-678.
42 A. W. Sleight, *Annu. Rev. Mater. Sci.*, 1998, **28**, 29-43.
43 A. L. Goodwin and C. J. Kepert, *Phys. Rev. B*, 2005, **71**, 140301.
44 K. W. Chapman, P. J. Chupas and C. J. Kepert, *J. Am. Chem. Soc.*, 2006, **128**, 7009-7014.
45 K. W. Chapman, P. J. Chupas, and C. J. Kepert, *J. Am. Chem. Soc.*, 2005, **127**, 15630-15636.
46 A. Sanson, J. Synchrotron Radiat., 2008, 15, 514–518.